Nano Research

Open Access

Research Article

Biomimetic hybrid membranes-camouflaged biosynthesized melanin nanoparticles for efficient cancer photothermal-immunotherapy

Jiayingzi Wu[1,§], Jiahui Li[1,§], Meng Wang[1], Peijia Ma[1], Hengke Liu[1], Jing Lin[1] ✉, Fei Yan[2,3] ✉, and Peng Huang[1] ✉

[1] *Marshall Laboratory of Biomedical Engineering, International Cancer Center, Guangdong Key Laboratory for Biomedical Measurements and Ultrasound Imaging, Laboratory of Evolutionary Theranostics (LET), School of Biomedical Engineering, Shenzhen University Medical School, Shenzhen University, Shenzhen 518055, China*

[2] *CAS Key Laboratory of Quantitative Engineering Biology, Shenzhen Institute of Synthetic Biology, Shenzhen Institutes of Advanced Technology, Chinese Academy of Sciences, Shenzhen 518055, China*

[3] *University of Chinese Academy of Sciences, Beijing 100049, China*

[§] *Jiayingzi Wu and Jiahui Li contributed equally to this work.*

Cite this article: *Nano Research*, **2026**, *19*, 94908589. https://doi.org/10.26599/NR.2026.94908589

ABSTRACT: Biomimetic membranes-camouflaged nanomedicines show promising potential in cancer therapy. Herein, we developed biomimetic hybrid membranes-camouflaged biosynthesized melanin nanoparticles, termed MBM-PM, by co-extruding near-infrared (NIR) light-absorbing melanin nanoparticles naturally enveloped in bacterial outer membranes (MBM) with programmed cell death protein 1 (PD-1)-expressing mammalian cell membrane nanovesicles (PM), for efficient cancer photothermal-immunotherapy. The melanin core within the outer membrane vesicles (OMV) generates a photothermal effect, inducing thermal stress to directly kill cancer cells and triggering immunogenic cell death (ICD), which enhances antitumor immunity. Furthermore, the pathogen-associated molecular patterns (PAMPs) present in the bacterial membrane component of MBMs stimulate a robust antitumor immune response. The PM components not only confer cancer cell-targeting capability but also block the PD-1/programmed death-ligand 1 (PD-L1) interaction, further enhancing immune activation. Our studies demonstrate that the MBM-PM nanoplatform can effectively eradicate primary tumors and significantly inhibit distant tumors and lung metastasis, offering a promising biosynthesized nanoplatform for cancer photothermal-immunotherapy.

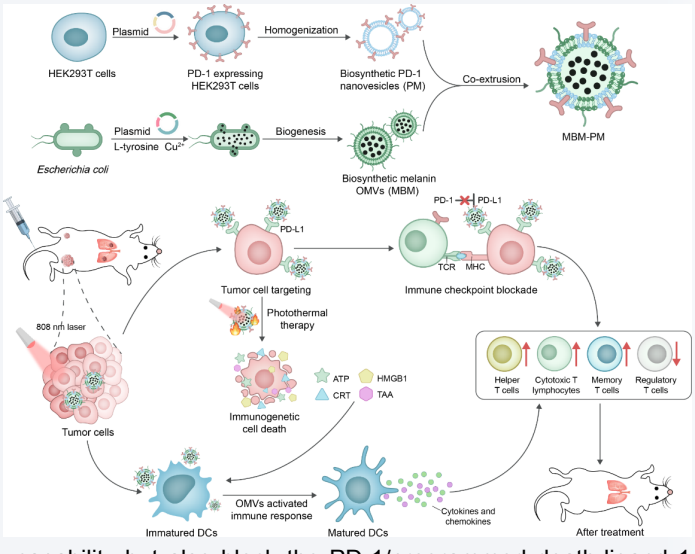

KEYWORDS: biomimetic membranes, biosynthesized nanoparticles, photothermal therapy, immunotherapy, cancer

1 Introduction

Tumor immunotherapies have revolutionized traditional methods by harnessing the host immune system to combat tumors [1, 2]. Despite their promise, clinical response rates remain low, primarily due to the immunosuppressive tumor microenvironment and tumor heterogeneity [3, 4]. Single-pathway targeted treatments often fail to fully activate immune cell functions, leading to suboptimal therapeutic outcomes. Additionally, systemic administration of immunotherapeutic agents can result in non-specific distribution, limiting efficacy and causing severe off-target toxicity. Therefore, it is crucial to develop combinational cancer

Received: November 16, 2025; **Revised:** February 12, 2026
Accepted: February 22, 2026

✉Address correspondence to Peng Huang, peng.huang@szu.edu.cn; Fei Yan, fei.yan@siat.ac.cn; Jing Lin, jingl@szu.edu.cn

immunotherapeutic strategies to enhance therapeutic efficacy while reducing potential off-target toxicity [5–7]. Recently, combining photothermal therapy (PTT) with immunotherapy has gained significant attention. This light-based approach offers high spatiotemporal precision, minimal invasiveness, and reduced off-target toxicity [8]. Initially aimed at tumor destruction, PTT is now recognized for inducing immunogenic cell death (ICD), which releases damage-associated molecular patterns (DAMPs) [8–10]. These DAMPs enhance the immunogenicity of the tumor microenvironment, boosting the immune response against cancer [9–12]. Various nanomaterials composed of photothermal conversion agents and immunotherapeutic agents have been developed as co-delivery systems for photothermal immunotherapy [7]. The typical photothermal conversion agents include noble metallic nanoparticles [13], quantum dots [14], carbon-based nanoparticles [15], polymer nanoparticles [16–18] and small molecule dyes [19]. However, chemically synthesized compounds always require complex synthesis processes and pose concerns about limited loading efficiency, biocompatibility, stability and drug leakage during blood circulation [20].

In contrast to the chemically synthesized compounds, outer membrane vesicles (OMVs) are natural products derived from bacteria and provide advantages such as superior biodegradability, enhanced biocompatibility, extended blood circulation time, and improved stability in circulation [21, 22]. More importantly, these nanovesicles contain various pathogen-associated molecular patterns (PAMPs) [23], including peptidoglycan, lipopolysaccharide, and flagellin, not only activating innate immune signaling pathways but also inducing adaptive immune responses [22, 24–27]. Due to these merits, OMVs have been utilized as immunoadjuvants and delivery vehicles for combinational immunotherapy, with synthetic photothermal agents and/or immunotherapeutic agents loaded inside or absorbed on their surface [28–30]. Although these hybrid nanomaterials have demonstrated the potential of OMVs as excellent nanocarriers with intrinsic immunomodulatory properties, biomaterials-based OMVs with photothermal effects have been scarcely reported. One example is the recent development of biosynthesized gold nanoparticles coated with bacterial membrane components, which successfully activate the immune response and elicit localized light-converting hyperthermia, thereby enhancing anti-tumor efficacy [31].

However, challenges such as short absorption wavelength, the need for repeated dosages, and non-specific targeting remain to be addressed.

In this study, we employed biosynthetic methods to produce near-infrared (NIR) light-absorbing melanin nanoparticles naturally enveloped in bacterial outer membranes (MBM) [32–34], which provide a photothermal effect capable of inducing ICD and exhibit potent immunoadjuvant properties. Furthermore, by hybridizing MBM with PD-1-engineered eukaryotic membranes (PM), we constructed a dual-functional prokaryote-eukaryocyte membranes (MBM-PM) (Fig. 1). This design not only enhances tumor-specific accumulation via the PD-1/PD-L1 axis but also provides a localized checkpoint blockade, which, in concert with ICD, promotes the conversion of the "cold" tumor into an "immunologically hot" one [35, 36]. Consequently, this targeted photothermal and immunoactive system enables the complete

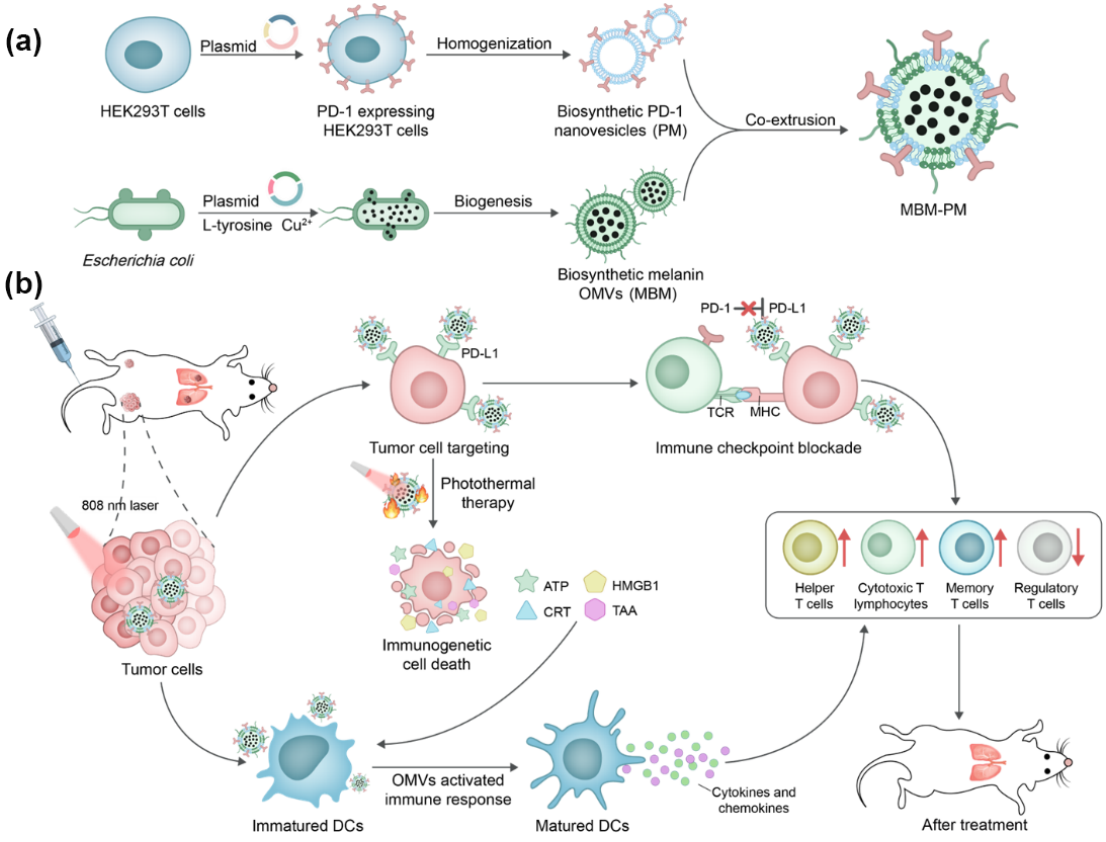

Figure 1 Schematic illustration of the MBM-PM-mediated cancer photothermal-immunotherapy. (a) Fabrication of MBM-PM through biosynthesis. (b) Mechanism of antitumor immune response by MBM-PM-mediated photothermal-immunotherapy. ATP: adenosine triphosphate, HMGB1: high-mobility group box 1 protein, TAA: tumor-associated antigen, DC: dendritic cell, TCR: T-cell receptor, MHC: major histocompatibility complex.

eradication of primary tumors and efficient inhibition of distant tumors and lung metastasis without obvious systemic adverse effects.

2 Experimental

2.1 Materials

L-tyrosine and $CuSO_4·5H_2O$ were purchased from Sigma-Aldrich (USA). Dulbecco's modified Eagle medium (DMEM) and fetal bovine serum (FBS) were provided by Gibco (USA). Hoechst 33342 was obtained from APExBIO Technology (USA). ATP Assay Kit was obtained from Beyotime Biotechnology Co. (Shanghai, China). Alexa Fluor® 647 (Cat. ab203848), anti-Calreticulin (Cat. ab92516), and anti-HMGB1 (Cat. ab79823) were purchased from Abcam (UK). Anti-CD16/32 (Cat. 101302), Zombie Aqua™ Fixable Viability kit (Cat. 423102), anti-CD45-Pacific Blue (Cat. 103125), anti-CD3-FITC (Cat. 100204), anti-CD4-APC-CY7 (Cat. 100414), anti-CD8a-PE-CY7 (Cat. 100721), anti-CD25-APC (Cat. 102012), anti-Foxp-PE (Cat. 126404), anti-CD80-PE (Cat. 104707), anti-CD86-APC (Cat. 105012), anti-CD11c-Pacific Blue (Cat. 117321), anti-MHC-II-PE-CY7 (Cat. 107630), anti-CD62L-PE (Cat. 104407), and anti-CD44-APC (Cat. 103012) were purchased from Biolegend (USA). 4T1 cell lines were purchased from Cell Bank of Chinese Academy of Sciences (China).

2.2 Characterization

Dynamic light scattering (DLS) and zeta potential measurements were performed using a Malvern Nano-zetasizer. Ultraviolet–visible–NIR (UV–vis–NIR) spectra were recorded with Cary-60 (Agilent Technologies, Inc., USA). Transmission electron microscopic images were obtained with an HT7700 microscope (HITACH, Ltd., Japan).

2.3 Synthesis of PM

Firstly, HEK293T cells were transfected with a plasmid expressing PD-1/enhanced green fluorescent protein (EGFP) fusion protein, and then screened with hygromycin B for two weeks to obtain a PD-1/EGFP stably expressing cell line. The expression of PD-1 protein was verified using fluorescence imaging. To collect the cell membrane, PD-1/EGFP stably expressing HEK293T cells were cultured in eight 75 cm^2 flasks for 24 h before being digested by trypsin and centrifuged to collect the cells (1500 rpm, 5 min). After washing with PBS for three times, the cell pellets were dissolved in HEPES-MOPS (HM) buffer (0.25 mM sucrose, 1 mM ethylenediaminetetraacetic acid (EDTA), 20 mM Hepes-NaOH, protease inhibitor, pH = 7.4) and homogenized on ice. The cell debris was then centrifuged (1500 rpm, 5 min) to remove the cell pellets, and then centrifuged (7500 rpm, 20 min) to remove organelles. Cell membrane fragments were collected by centrifugation (20,000×*g*, 60 min). Finally, membrane nanovesicles were obtained after being successively filtered using 0.8, 0.45, and 0.22 μm membrane filters and lyophilized for long-term storage.

2.4 Synthesis of melanin nanoparticles (MNP)

Plasmids encoding Tyr1 were transformed into *E. coli* DH5*α* competent cells (BC102-01, Biomed) and grown in 3 mL Luria Broth (LB) medium supplemented with 50 μg·mL^{-1} ampicillin for overnight at 37 °C (the first cultivation). Large-scale cultures (200 mL) in LB medium containing 50 μg·mL^{-1} ampicillin were inoculated at a ratio of 1:100 with the overnight culture for 24 h at 37 °C (the second cultivation). The second cultivation was continuously inoculated for 6 h supplemented with 50 μg·mL^{-1} $CuSO_4·5H_2O$ and 0.8 mg·mL^{-1} L-tyrosine. Then, the culture both were centrifuged for 10 min at 8000 rpm. The black supernatant was used for melanin purification and passed through a Millipore 0.22 μm polyethersulfone membrane, according to the previous method [37]. The supernatant was added with a one-third volume of 6 M HCl and left at room temperature for 10 h. Then, the supernatant was centrifuged for 10 min at 12,000 rpm to collect melanin nanoparticles. Finally, MNP was washed with deionized water and lyophilized into black powder. MNP was dissolved in the appropriate amount of ammonia solution (25%–28%) and then ammonium was evaporated by rotary evaporation to obtain MNP solution.

2.5 Synthesis of MBM

Plasmids encoding Tyr1 were transformed into *E. coli* DH5*α* competent cells (BC102-01, Biomed) and grown in 3 mL LB medium supplemented with 50 μg·mL^{-1} ampicillin for overnight at 37 °C (the first cultivation). Large-scale cultures (200 mL) in LB medium containing 50 μg·mL^{-1} ampicillin were inoculated at a ratio of 1:100 with the overnight culture for 24 h at 37 °C (the second cultivation). The second cultivation was continuously inoculated for 6 h supplemented with 50 μg·mL^{-1} $CuSO_4·5H_2O$ and 0.8 mg·mL^{-1} *L*-tyrosine. Then, the culture liquid was centrifuged for 10 min at 8000 rpm. The supernatant was centrifuged three times and then filtered through 0.8, 0.45 and 0.22 μm membrane filters before being ultrafiltered via a 100 kDa ultrafiltration tube. MBM was collected ultracentrifugation at 150,000×*g* for 2 h at 4 °C. The collected MBM were washed with PBS using centrifugation at 150,000×*g* for 2 h at 4 °C, then finally resuspended in 400 μL PBS and stored at −20 °C until use.

2.6 Synthesis of MBM-PM

PM (0.5 mL, 3 mg·mL^{-1}) and MBM (0.5 mL, 3 mg·mL^{-1}) are mixed at a mass ratio of 1:1 and extruded through a 0.22 μm filter membrane. Then, the mixture was extruded 30 times through a 0.2 μm filter membrane to obtain the MBM-PM.

2.7 *In vitro* photothermal study

To measure the concentration dependent photothermal effect, MBM-PM was dissolved in PBS solution at varying concentrations (0, 50, 100, or 200 μg·mL^{-1}) with laser irradiation (808 nm, 0.8 W·cm^{-2}, 8 min) and the temperature changes were monitored by infrared thermal imaging camera (FLIR A310). To determine the laser density dependent photothermal effect, MBM-PM dissolved in PBS solution was irradiated with 808 nm laser (laser density: 0.4, 0.6, 0.8 and 1.0 W·cm^{-2}) and the temperature changes were monitored. To measure photothermal cycles and photothermal conversion efficiency, MBM-PM dissolved in PBS was treated with NIR laser (808 nm, 0.8 W·cm^{-2}, 8 min) and cooled naturally for 8 min, repeated 5 cycles, then the temperature changes were recorded.

2.8 Cell culture

4T1 cells were cultured in DMEM supplemented 10% FBS. The cells were maintained in a humid environment containing 5% CO_2 at 37 °C.

2.9 *In vitro* cellular uptake

4T1 cells were plated at an initial density of 1×10^4 cells per well in 96-well CellCarrier™ microplates (PerkinElmer) and incubated at 37 °C and under 5% CO_2 atmosphere for overnight. For labeling, the cells were incubated with Hoechst 33342 for another 10 min. DMEM containing RhB-labeled MNP (50 μg·mL^{-1}) , RhB-labelled MBM (50 μg·mL^{-1}) , RhB-labeled MBM hybridized with HEK293T cell membrane (MCM) (50 μg·mL^{-1}) and RhB-labeled MBM-PM (50 μg·mL^{-1}) were used to replace the media. Cellular uptake was then observed using a high content analysis system (Operatta CLS).

2.10 Cytotoxicity test

4T1 cells were plated at an initial density of 1×10^4 cells per well on 96 well plates and incubated at 37 °C and under 5% CO_2 atmosphere overnight. The cells were incubated in the fresh media containing MNP, MBM or MBM-PM (0, 25, 50, 100 or 200 μg·mL^{-1}) for 24 h. Cell proliferation was evaluated by using cell counting kit 8 (CCK8) according to the manufacturer's instructions. Three replicates were performed for each group.

2.11 *In vitro* PTT assay

4T1 cells were plated at an initial density of 1×10^4 cells per well on 96 well plates and incubated at 37 °C and under 5% CO_2 atmosphere for overnight. The cells were incubated in the fresh media containing MNP, MBM or MBM-PM (0, 50, 100, 150 or 200 μg·mL^{-1}) for 8 h. Afterward, 808 nm laser (0.8 W·cm^{-2}) was used to irradiate the cells for 6 min. After further incubation for 16 h, cell proliferation was evaluated by using CCK8 according to the manufacturer's instructions. Three replicates were performed for each group.

2.12 Live–dead cell staining

4T1 cells were plated at an initial density of 1×10^4 cells per well on 96 well plates and incubated at 37 °C and under 5% CO_2 atmosphere for overnight. The cells were incubated in the fresh media containing MNP, MBM or MBM-PM (200 μg·mL^{-1}) for 8 h. Afterward, 808 nm laser (0.8 W·cm^{-2}) was used to irradiate the cells for 6 min. Under the same experimental condition, cells that did not undergo laser irradiation were used as control groups. After further incubation for 12 h, the cells of each group were incubated with calcein acetoxymethyl ester (CA) (1 μg·mL^{-1}) and propidium iodide (PI) (2 μg·mL^{-1}) staining reagents for 20 min and then observed using a Nikon Eclipse Ts2 inverted fluorescence microscope.

2.13 Calreticulin (CRT) detection

4T1 cells were plated at an initial density of 1.5×10^5 cells per well into confocal dishes and incubated at 37 °C and under 5% CO_2 atmosphere for overnight. The cells were incubated in the fresh media containing MNP, MBM or MBM-PM (200 μg·mL^{-1}) for 8 h. Afterward, 808 nm laser (0.8 W·cm^{-2}) was used to irradiate the cells for 6 min. Under the same experimental condition, cells that did not undergo laser irradiation were used as control groups. After further incubation for 4 h, cells were fixed with 4% paraformaldehyde and incubated overnight with anti-Calreticulin (Cat. ab92516) at 4 °C and then incubated with Alexa Fluor® 647 (Cat. ab203848) for 1 h. Then, cell nuclei were stained with Hoechst 33342. Finally, the cells were observed by confocal fluorescence microscopy.

2.14 HMGB1 detection

4T1 cells were plated at an initial density of 1.5×10^5 cells per well into confocal dishes and incubated at 37 °C and under 5% CO_2 atmosphere for overnight. The cells were incubated in the fresh media containing MNP, MBM or MBM-PM (200 μg·mL^{-1}) for 8 h. Afterward, 808 nm laser (0.8 W·cm^{-2}) was used to irradiate the cells for 6 min. Under the same experimental condition, cells that did not undergo laser irradiation were used as control groups. After further incubation for 4 h, cells were fixed with 4% paraformaldehyde, broken by 0.25% Triton X-100 and incubated overnight with anti-HMGB1 (Cat. ab79823) at 4 °C and then incubated with Alexa Fluor® 647 (Cat. ab203848) for 1 h. Then, the cell nuclei were stained with Hoechst 33342. Finally, the cells were observed by confocal fluorescence microscopy.

2.15 ATP detection

4T1 cells were plated at an initial density of 2×10^5 cells per well into 6-well plate and incubated at 37 °C and under 5% CO_2 atmosphere for overnight. The cells were incubated in the fresh media containing MNP, MBM or MBM-PM (200 μg·mL^{-1}) for 12 h. Afterward, 808 nm laser (0.8 W·cm^{-2}) was used to irradiate the cells for 6 min. Under the same experimental condition, cells that did not undergo laser irradiation were used as control groups. After further incubation for 20 h, the supernatants were collected and measured by ATP assay kit.

2.16 Animals

Female Balb/c mice aged 4–6 weeks were purchased from Guangdong Medicinal Laboratory Animal Center (Guangzhou, China) and were conducted in accordance with the regulations of the Animal Ethical and Welfare Committee of Shenzhen University (AEWC-SZU, maximal tumor size: < 2×10^3 mm^3). All of the experimental mice were housed under standard conditions (temperature: ~ 22 °C, humidity: 40%–70%, 12 h dark–light cycles) with free access to sterile food and water.

2.17 *In vivo* PA imaging

4T1 cells (2×10^6) were subcutaneously injected into the right flank of Balb/c mice to establish the subcutaneous tumor model. *In vivo* PA imaging was performed when tumor volume reached ~ 150 mm^3. PA imaging was carried out with a commercial multimodal PA imaging system (Vevo LAZR-X, FUJIFILM Visualsonics, Inc.). Tumors-bearing mice were anesthetized using 2% isoflurane in oxygen delivered through a nose cone, and their body temperature was maintained by a heat pad during the PA imaging period. PA images of 4T1 tumors (0 h) and 1, 2, 4, 6, 8, 12, and 24 h after intravenous injection of 100 μL of MNP, MBM, MCM or MBM-PM (15 mg·kg^{-1}) were collected, respectively.

2.18 *In vivo* antitumor efficiency

The mice were divided into groups randomly. For the first (primary) tumor inoculation, 4T1 cells (2×10^6) suspended in serum-free DMEM solution were subcutaneously injected into the right flank of each female Balb/c mouse. For the second (distant) tumor inoculation that was conducted after 5 days, 4T1 cells (5×10^5) suspended in serum-free DMEM solution were subcutaneously injected into the left flank of each female Balb/c mouse. 1 day after distant tumor inoculation, mice were injected intravenously with PBS, MNP, MBM, or MBM-PM (15 mg·kg^{-1}, n = 5). After 8 h of

injection, the photothermal groups of mice were irradiated with 808 nm laser (0.8 W·cm^{-2}, 10 min). An infrared thermal camera (FLIR A310) was used to check the tumor temperatures. Subsequently, volumes of both types of tumors as well as mouse body weights were monitored every subsequent day.

2.19 Histological studies

On day 3 after different therapeutics, mice were euthanized, and primary tumors were then fixed in formalin solution (4%). As-obtained tumor tissue sections were stained with hematoxylin and eosin (H&E), TUNEL (terminal deoxynucleotidyl transferase dUTP nick end labeling), CRT, HMGB1, PD-L1 and heat shock protein 70/90 (HSP70/90). On day 14 after different therapeutics, mice were euthanized, and tumors along with other harvested organs were then fixed in formalin solution (4%). Both primary and distant tumor slices were stained for IL-1β, Caspase-3, CD4$^+$/CD8$^+$ and Granzyme B immunofluorescence analysis. Organ slices were stained for H&E analysis.

2.20 Anti-metastasis efficacy evaluation

After 28 days of treatment, the mice in PBS and MBM-PM+L group (n = 3) were euthanized to extract lungs. The lungs were analyzed by H&E staining.

2.21 Immune response analysis

For DC maturation, the tumor-draining lymph nodes (TDLNs) were separated on day 3 and grinded into cell suspensions using the blunt end of a 1 mL syringe. Then, the cell suspensions were filtered through a cell strainer (pore size: 70 μm) to remove the large cell debris. The as prepared single cell suspensions were incubated with anti-CD16/32 (Cat. 101302, Biolegend) to block Fc receptors and then stained with fluorescence-labelled antibodies according to the vendors's protocols, including Zombie Aqua™ Fixable Viability kit (Cat. 423102, Biolegend), anti-CD80-PE (Cat. 104707, Biolegend), anti-CD86-APC (Cat. 105012, Biolegend), anti-CD11c-Pacific Blue (Cat. 117321, Biolegend), and anti-MHC-II-PE-CY7 (Cat. 107630, Biolegend). The stained cells were stored in the dark for flow cytometric analysis (Beckman Coulter, USA).

For cytotoxic T lymphocytes (CTLs) evaluation, distant tumors in different groups were collected on day 14 and cut into 1 mm^3 pieces. The tissue pieces were digested using a mixed enzyme solution (250 U·mL^{-1} collagenase IV, 100 U·mL^{-1} hyaluronidase, and 100 U·mL^{-1} neutral protease) at 37 °C for 15 min under mild stirring. Afterwards, the tumor tissues were filtered through a cell strainer (pore size: 70 μm) to remove the large cell debris. The as-prepared single cell suspensions were incubated with anti-CD16/32 (Cat. 101302, Biolegend) to block Fc receptors and then stained with fluorescence-labelled antibodies according to the vendors's protocols, including Zombie Aqua™ Fixable Viability kit (Cat. 423102, Biolegend), anti-CD45-Pacific Blue (Cat. 103125, Biolegend), anti-CD3-FITC (Cat. 100204, Biolegend), anti-CD4-APC-CY7 (Cat. 100414, Biolegend), anti-CD8a-PE-Cy7 (Cat. 100721, Biolegend), anti-CD25-APC (Cat. 102012, Biolegend), and anti-Foxp-PE (Cat. 126404, Biolegend). The stained cells were stored in the dark for flow cytometric analysis (Beckman Coulter, USA).

For effector memory T cell evaluation, the spleens were harvested from the tumor-bearing mice, homogenized, and treated with ACK Lysing Buffer (Biolegend) to remove the red blood cells. The as prepared single cell suspensions were incubated with anti-CD16/32 (Cat. 101302, Biolegend) to block Fc receptors and then stained with fluorescence-labelled antibodies according to the vendors's protocols, including Zombie Aqua™ Fixable Viability kit (Cat. 423102, Biolegend), anti-CD45-Pacific Blue (Cat. 103125, Biolegend), anti-CD3-FITC (Cat. 100204, Biolegend), anti-CD4-APC-CY7 (Cat. 100414, Biolegend), anti-CD8a-PE-Cy7 (Cat. 100721, Biolegend), anti-CD62L-PE (Cat. 104407, Biolegend), and anti-CD44-APC (Cat. 103012, Biolegend). The stained cells were stored in the dark for flow cytometric analysis (Beckman Coulter, USA). To test the tumor necrosis factor-α (TNF-α), IL-6, interferon-γ (IFN-γ) and IL-1β in serum, blood samples were collected on day 3 and analyzed by enzyme-linked immunosorbent assay (ELISA).

2.22 Statistical analysis

The quantitative data analysis was manifested as mean ± standard deviation (SD). Unpaired two-sided t-test with unequal variance, one-way ANOVA with a Tukey post-hoc test or log-rank test was applied to test the significance of the difference. n.s.: no significant difference; *P < 0.05; **P < 0.01; ***P < 0.001; and ****P < 0.0001.

3 Results and discussion

3.1 Biosynthesis and characterization of MBM-PM

To obtain NIR-absorbing OMVs with photothermal conversion capability, the recombinant plasmid containing tyrosinase (Tyr1) gene was introduced into DH5α *Escherichia coli* (*E. coli*) strains [34]. With the supplementation of $CuSO_4$ and *L*-tyrosine, the genetically engineered *E. coli* strains produced a substantial amount of melanin, which would be packaged into the membrane and cytosol of OMVs (MBM) and sequentially shed into the culture medium [38]. In addition, PD-1-expressing HEK293T cells were also established through gene editing, and the PD-1-expressed cell membrane nanovesicles (PM) were collected after homogenization (Fig. S1 in the ESM). Finally, the two biosynthesized nanovesicles were hybridized through co-extrusion [37, 39], creating biomaterials-based photothermal conversion agents encapsulated by prokaryote-eukaryocyte hybrid membranes (MBM-PM). The colloidal and optical properties of MBM-PM were studied and compared with those of MBM. Transmission electron microscopy (TEM) imaging (Figs. 2(a) and 2(b)) and DLS analysis (Fig. 2(c)) revealed that MBM-PM was spherical structure and good dispersibility. The size of MBM-PM (129.0 ± 3.4 nm) was slightly larger than that of MBM (113.8 ± 3.5 nm), likely due to the co-extrusion process, which combined components from both types of vesicles, resulting in size increase. Zeta potential measurements indicated a relatively more negative surface charge for MBM-PM (−20.8 ± 1.8 mV) compared to MBM (−18.8 ± 0.9 mV), reflecting the existence of the PM components (−25.4 ± 0.6 mV) after co-extrusion (Fig. 2(d)). Both MBM and MBM-PM demonstrated broad absorption in the NIR range (Fig. 2(e)), due to the presence of melanin as an NIR absorber. These results confirm the successful fabrication of MBM-PM, featuring an NIR-absorbing core and a hybrid membrane surface.

Next, the photothermal property of MBM-PM was evaluated. A concentration gradient of MBM-PM solution was exposed to an 808 nm laser at a fixed laser power density of 0.8 W·cm^{-2}, and the results showed that the photothermal effect was strongly concentration dependent (Fig. 2(f)). After laser irradiation for 8 min, 200 μg·mL^{-1} MBM-PM solution could reach 53.2 °C, while the control group remained at 29.0 °C, indicating good

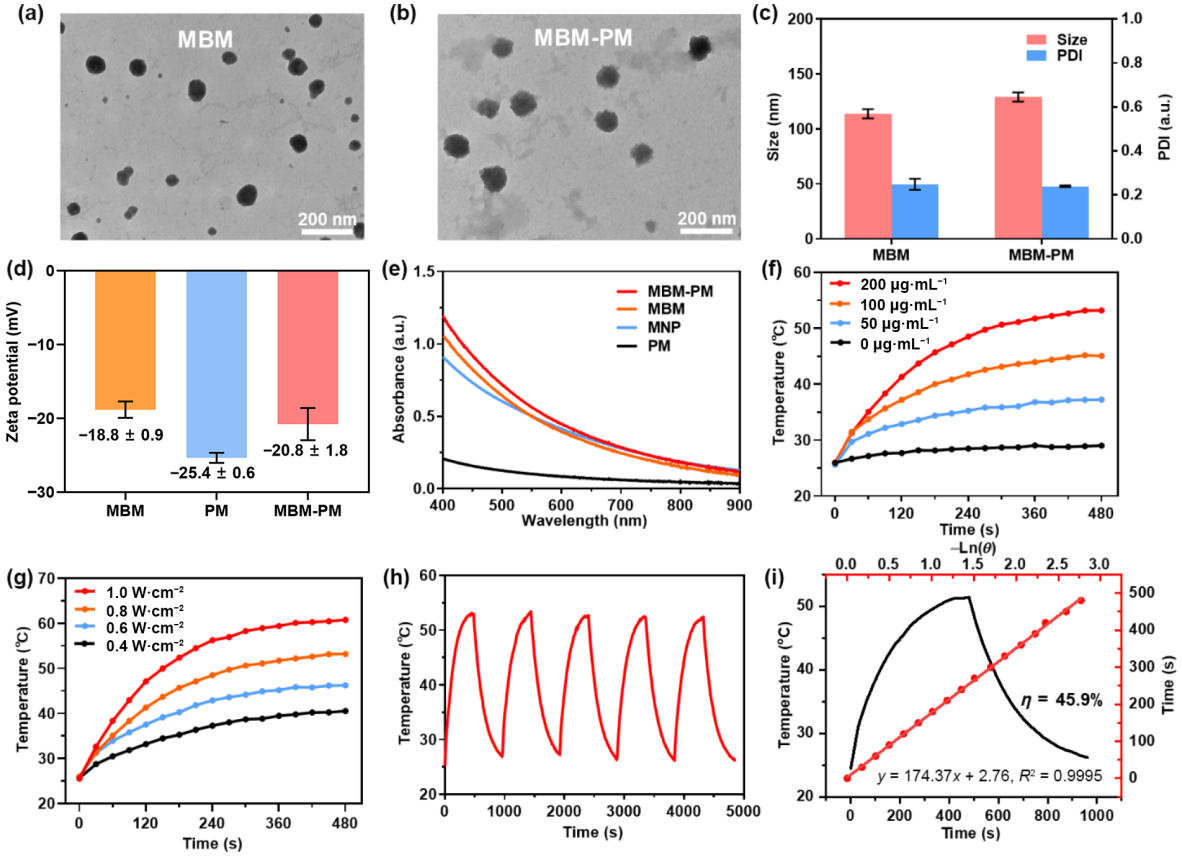

Figure 2 Biosynthesis and characterization of MBM-PM. Representative transmission electron microscopic images of (a) MBM and (b) MBM-PM. (c) Size distribution and polydispersity index (PDI) of MBM and MBM-PM (n = 3). (d) Zeta potential measurements of MBM, PM and MBM-PM (n = 3). (e) Absorption spectra of PM, MNP, MBM and MBM-PM. (f) Temperature change of MBM-PM with various concentrations (0–200 μg·mL^{-1}) under 808 nm laser irradiation (0.8 W·cm^{-2}). (g) Temperature change of MBM-PM (200 μg·mL^{-1}) under 808 nm laser irradiation with different power density (0.4–1.0 W·cm^{-2}). (h) Photothermal heating and natural cooling cycles of MBM-PM (200 μg·mL^{-1}) under the 808 nm laser irradiation (0.8 W·cm^{-2}). (i) Calculation of photothermal conversion efficiency. Black curve: Temperature change of MBM-PM (200 μg·mL^{-1}) under 808 nm laser irradiation for one on/off cycle. Red curve: Linear time data versus −Lnθ obtained from the cooling period, R^2 > 0.99. Data were expressed as mean ± SD.

photothermal conversion capability of MBM-PM. Also, a laser power-dependent temperature increase was observed with a constant concentration of 200 μg·mL^{-1} (Fig. 2(g)). In addition, MBM-PM presented good photothermal stability as its maximum temperatures retained nearly unchanged after five circles of heating and natural cooling (Fig. 2(h)). Furthermore, the photothermal conversion efficiency (η) of MBM-PM was calculated to be 45.9% (Fig. 2(i)), which is higher than the chemically synthesized melanin-like polydopamine (PDA) nanoparticles (16.6%–28.2%) [40, 41]. Taken together, we have demonstrated that MBM-PM is an efficient and stable photothermal conversion agent and would be promising for PTT.

3.2 *In vitro* photothermal cytotoxicity and induction of immunogenic cell death

At the cellular level, we first investigated the cellular uptake and targeting specificity of MBM-PM in the 4T1 cell line, which overexpresses PD-L1 (Fig. 3(a)). A fluorescent dye (Rhodamine B) was loaded into nanoparticles to obtain fluorescent derivatives for monitoring the cellular uptake process through fluorescence imaging. Compared to the control groups (MNP, MCM, and MBM), the cellular uptake of MBM-PM was much higher after 24 h incubation, demonstrating the crucial role of PD-1 in facilitating cellular binding and uptake (Fig. 3(b)). On the other hand, there was no noticeable difference in uptake among the control groups, indicating that the cell membrane alone does not influence cellular uptake.

Motivated by the good photothermal conversion and enhanced cellular uptake of MBM-PM, we then tested its photothermal cytotoxicity and compared it with MNP and MBM. Without laser irradiation, MNP, MBM and MBM-PM exhibited negligible cytotoxicity against 4T1 cells after 24-h incubation, even at a high concentration of 200 μg·mL^{-1} (Fig. 3(c)). However, upon laser irradiation, MBM-PM induced concentration-dependent cell death, which was more pronounced than that observed with MNP and MBM, both of which also possess photothermal properties (Fig. 3(d)). Specifically, at a concentration of 150 μg·mL^{-1}, the cell viability in the MBM-PM treated group decreased to 25.3%, while the MNP-treated and MBM-treated groups only showed reductions to 67.4% and 68.4%, respectively. At the same time, to visually assess the photothermal cytotoxicity, the cells were co-stained with CA and PI solutions to distinguish live (green fluorescence signal) and dead (red fluorescence signal) cells. As shown in Fig. 3(e), the combination of MBM-PM and laser irradiation induced the most dominant red fluorescence signal, suggesting the potent anticancer efficacy, while distinct green fluorescence signal was observed in control groups. The live/dead staining results were consistent with the above cytotoxicity tests, both of which underscore the potential

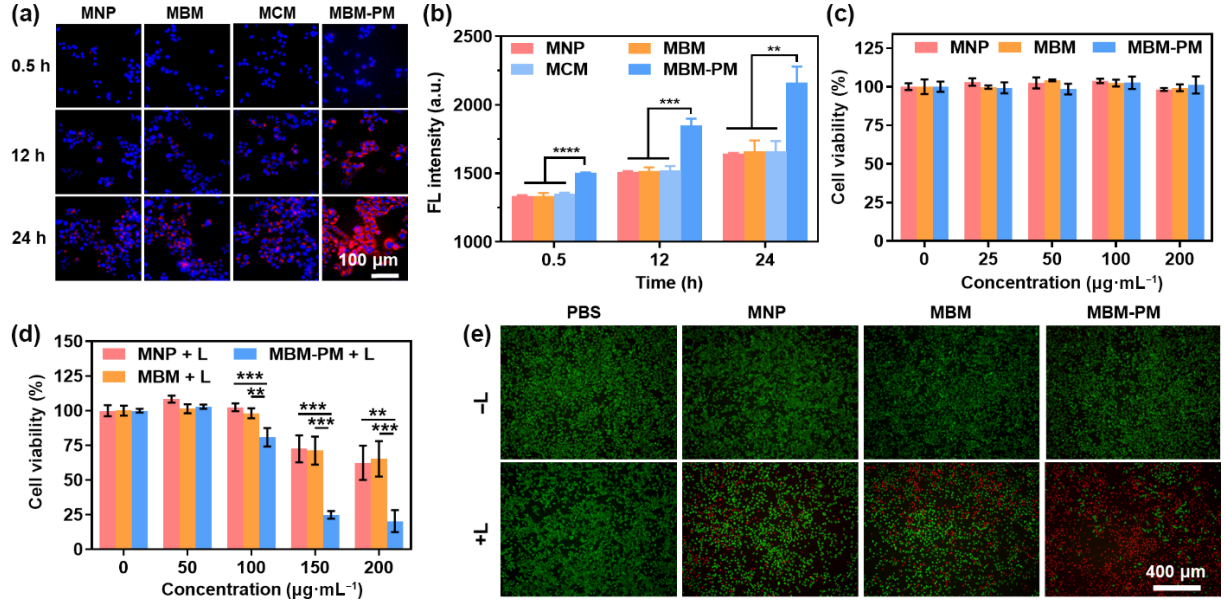

Figure 3 *In vitro* targeted photothermal cytotoxicity. (a) Time-dependent fluorescence images and (b) fluorescence intensity of 4T1 cells treated with 50 μg·mL^{-1} of MNP, MBM, MCM, or MBM-PM (n = 3). Cell nuclei were stained with Hoechst (blue) and nanoparticles were labeled with Rhodamine B (red). (c) Viability of 4T1 cells after 24-h incubation with MNP, MBM or MBM-PM at various concentrations (0–200 μg·mL^{-1}) (n = 3). (d) Viability of 4T1 cells after 24-h incubation with MNP, MBM or MBM-PM at various concentrations (0–200 μg·mL^{-1}) with 808 nm laser irradiation (0.8 W·cm^{-2}, 6 min) (n = 3). (e) Fluorescence images of 4T1 cells after 8-h incubation with PBS, MNP, MBM or MBM-PM with or without 808 nm laser irradiation (0.8 W·cm^{-2}, 6 min). Live cells were stained by Calcein-AM (green) and dead cells were stained by PI (red). Data were expressed as mean ± SD. Statistical significance was calculated via two-tailed Student's t-test. $^{**}P < 0.01$; $^{***}P < 0.001$; $^{****}P < 0.0001$.

of MBM-PM as an effective agent for targeted photothermal ablation, leveraging its superior uptake and photothermal conversion efficiency.

Besides the cell-killing capability, we further investigated whether the photothermal effect of MBM-PM can induce ICD, which is associated with the release of DAMPs, including surface-exposed CRT, secreted ATP, and passively released HMGB1. After incubation with PBS, MNP, MBM or MBM-PM, 4T1 cells were treated with or without laser irradiation and stained with anti-CRT or anti-HMGB1 antibodies for immunofluorescence imaging. As shown in Figs. 4(a) and 4(b), without laser irradiation, cells in different groups exhibited strong red fluorescence signals from anti-HMGB1 antibodies in the cell nucleus. After laser irradiation, the relative mean fluorescence intensities (MFIs) of anti-HMGB1 antibodies in MNP-, MBM-, and MBM-PM-incubated cells decreased by 47.6%, 48.0%, and 77.6%, respectively, compared with the unirradiated cells. The most dramatic decrease in fluorescence signal in MBM-PM-treated cells indicated the most significant release of HMGB1 from the nucleus. Additionally, the significantly promoted surface exposure of CRT was also observed (Figs. 4(c) and 4(d)). After laser irradiation, the relative MFIs of anti-CRT antibodies in MBM-PM-incubated cells increased by 3.1-fold, while MNP- and MBM-incubated cells showed increases of 2.5-fold and 2.4-fold, respectively. Moreover, the extracellular ATP level was evaluated using a chemiluminescence method, revealing a significant increase in the extracellular ATP levels within the MBM-PM group after laser irradiation (Fig. 4(e)). These results indicate that MBM-PM-mediated therapy can effectively induce ICD of 4T1 cancer cells.

3.3 *In vivo* photoacoustic imaging and photothermal conversion behavior

The tumor targeting capacities of biosynthetic nanoparticles were further evaluated through *in vivo* photoacoustic imaging (Figs. 5(a) and 5(b)). Comparative analysis demonstrated that biosynthetic cell membrane-coated nanoparticles, including MBM, MCM, and MBM-PM, all exhibited significantly greater tumor accumulation than naked melanin nanoparticles MNP. Notably, PD-1 hybrid membrane-coated MBM-PM nanoparticles demonstrated the highest tumor accumulation, indicating that PD-1-mediated targeting significantly enhanced nanoparticle enrichment in tumor tissues. This phenomenon could be attributed to the PD-1-driven active targeting mechanism.

Upon laser irradiation, the tumor surface temperatures for the MNP-, MBM- and MBM-PM-treated groups gradually increased to 41.8, 42.3 and 44.1 °C, respectively, while the PBS group only reached 38.9 °C (Figs. 5(c) and 5(d)). The higher temperature increase in the MBM-PM-treated group was attributed to its higher tumor accumulation, as indicated by the PA imaging results. Meanwhile, the relatively mild heating (< 45 °C) has the advantage of avoiding collateral damage to surrounding normal tissues and preventing unendurable heat pain in patients, while still being sufficient to induce ICD and increase vascular permeability [42–44].

3.4 *In vivo* anti-tumor efficacy and immune response

To further evaluate the anti-tumor efficacy and immune response *in vivo*, bilateral tumor models were established by subcutaneous inoculation of 4T1 cancer cells onto the right flank of Balb/c mice, followed by a second inoculation 5 days later on the left flank of the same mice (Fig. 6(a)). Based on the photoacoustic imaging results (Fig. 5(b)), laser irradiation was applied to the primary tumors 8 h after intravenous administration of PBS, MNP, MBM or MBM-PM. The size changes of primary and distant tumors were recorded after different treatments (Figs. 6(b)–6(e)). Without laser irradiation, MBM and MBM-PM could slightly impede the growth of both primary and distant tumors relative to PBS treatment. This

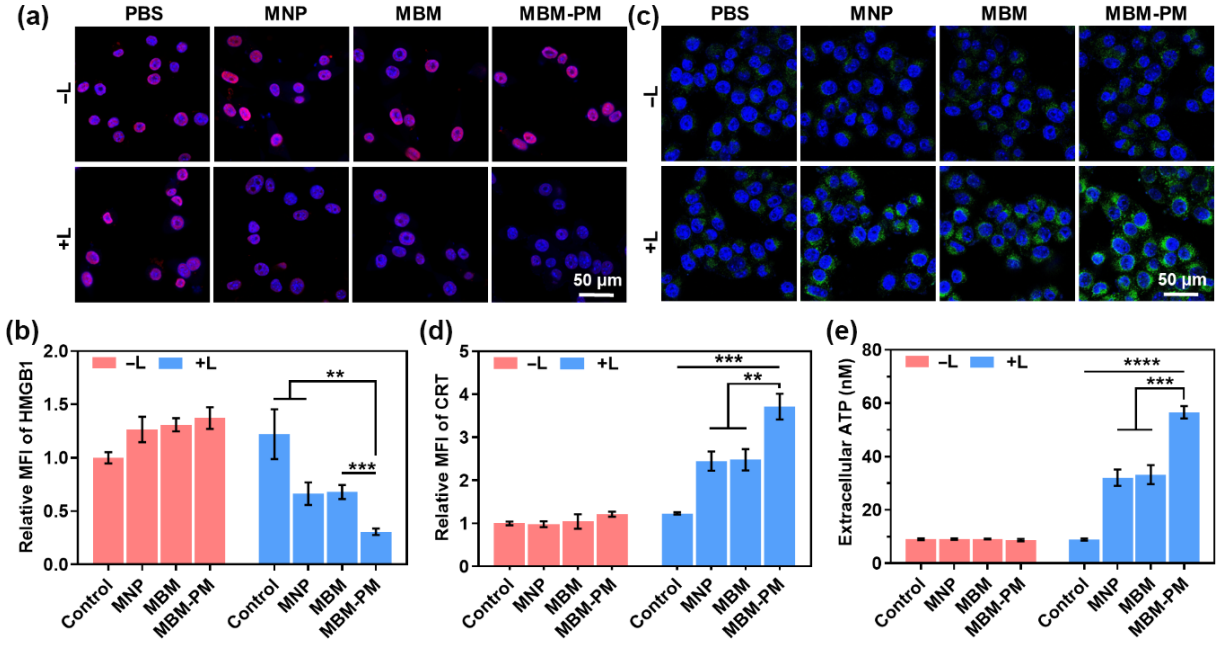

Figure 4 *In vitro* induction of immunogenic cell death. (a) HMGB1 immunofluorescence images and (b) relative MFIs of HMGB1 in 4T1 cells after the 8-h incubation with PBS, MNP, MBM or MBM-PM, with or without 808 nm laser irradiation (0.8 W·cm^{-2}, 6 min) (n = 3). Cell nuclei were stained with Hoechst (blue) and HMGB1 proteins were stained with anti-HMGB1 antibodies (red). (c) CRT immunofluorescence images and (d) relative MFIs of CRT in 4T1 cells after the 8-h incubation with PBS, MNP, MBM or MBM-PM with or without 808 nm laser irradiation (0.8 W·cm^{-2}, 6 min) (n = 3). Cell nuclei were stained with Hoechst (blue) and CRT proteins were stained with anti-CRT antibodies (green). (e) ATP secretion in 4T1 cells t after the 8-h incubation with PBS, MNP, MBM or MBM-PM with or without 808 nm laser irradiation (0.8 W·cm^{-2}, 6 min) (n = 3). Data were expressed as mean ± SD. Statistical significance was calculated via two-tailed Student's t-test. $^{**}P < 0.01$; $^{***}P < 0.001$; $^{****}P < 0.0001$.

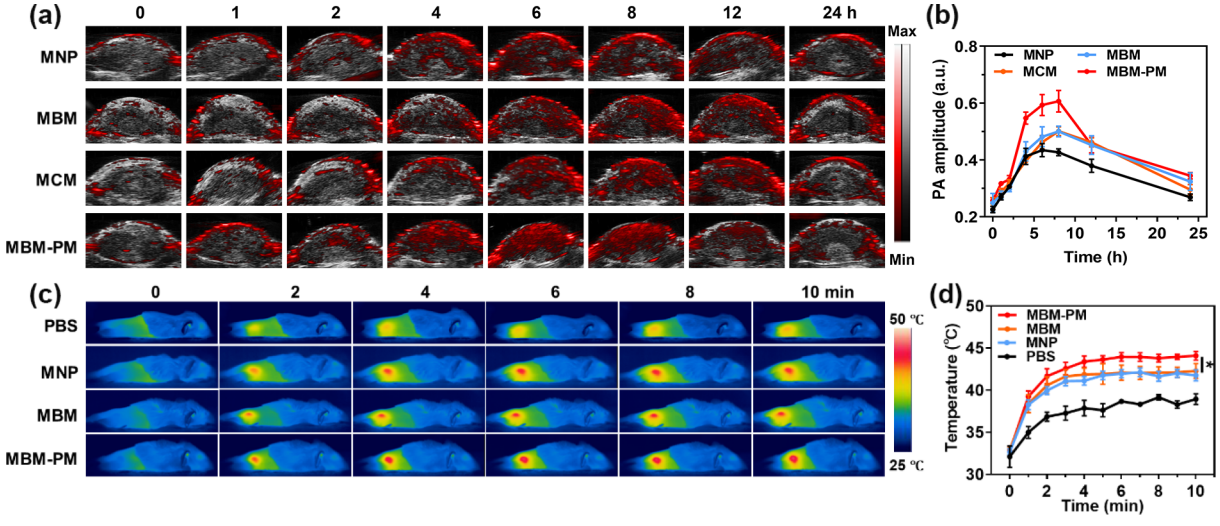

Figure 5 *In vivo* photoacoustic imaging and photothermal conversion behavior. (a) Representative photoacoustic images at 808 nm of 4T1 tumor on living mice at different time points after intravenous injection of MNP, MBM, MCM or MBM-PM. (b) Quantification of PA signal intensity within tumor region over time (n = 3). (c) Representative infrared thermal images of 4T1 tumor-bearing mice under 808 nm laser irradiation (0.8 W·cm^{-2}, 10 min) after intravenous injection of PBS, MNP, MBM or MBM-PM at a post-injection time of 8 h. (d) Averaged tumor temperature as a function of laser irradiation time after intravenous injection of PBS, MNP, MBM or MBM-PM at a post-injection time of 8 h (n = 3). Data were expressed as mean ± SD. Statistical significance was calculated via two-tailed Student's t-test. $^{*}P < 0.05$.

observation implies the immune response triggered by PAMPs on the membrane surface of OMV, and it could be further enhanced by the tumor-targeting and checkpoint-blockade function of PD-1 in MBM-PM. With laser irradiation, MNP, MBM, and MBM-PM competently restricted tumor growth in mice with enhanced inhibition rates. The primary tumors in the MBM-PM + laser irradiation group were nearly completely ablated, while tumor recurrence was observed in MNP- and MBM-treated mice after laser irradiation. In addition, similar to the primary tumor results, the MBM-PM + laser irradiation group achieved the most effective elimination of distant tumors, suggesting that the combination treatment amplifies the systemic anti-tumor immune response.

Besides, attributed to the synergistic antitumor effect, the mice treated with MBM-PM and laser irradiation reduced the rate of tumor progression and resulted in a significantly prolonged survival rate (Fig. 6(f)). Furthermore, the therapeutic effect was confirmed by H&E staining (Fig. 6(g)) of primary tumor tissues on day 3 after different treatments. The MBM-PM + laser irradiation group

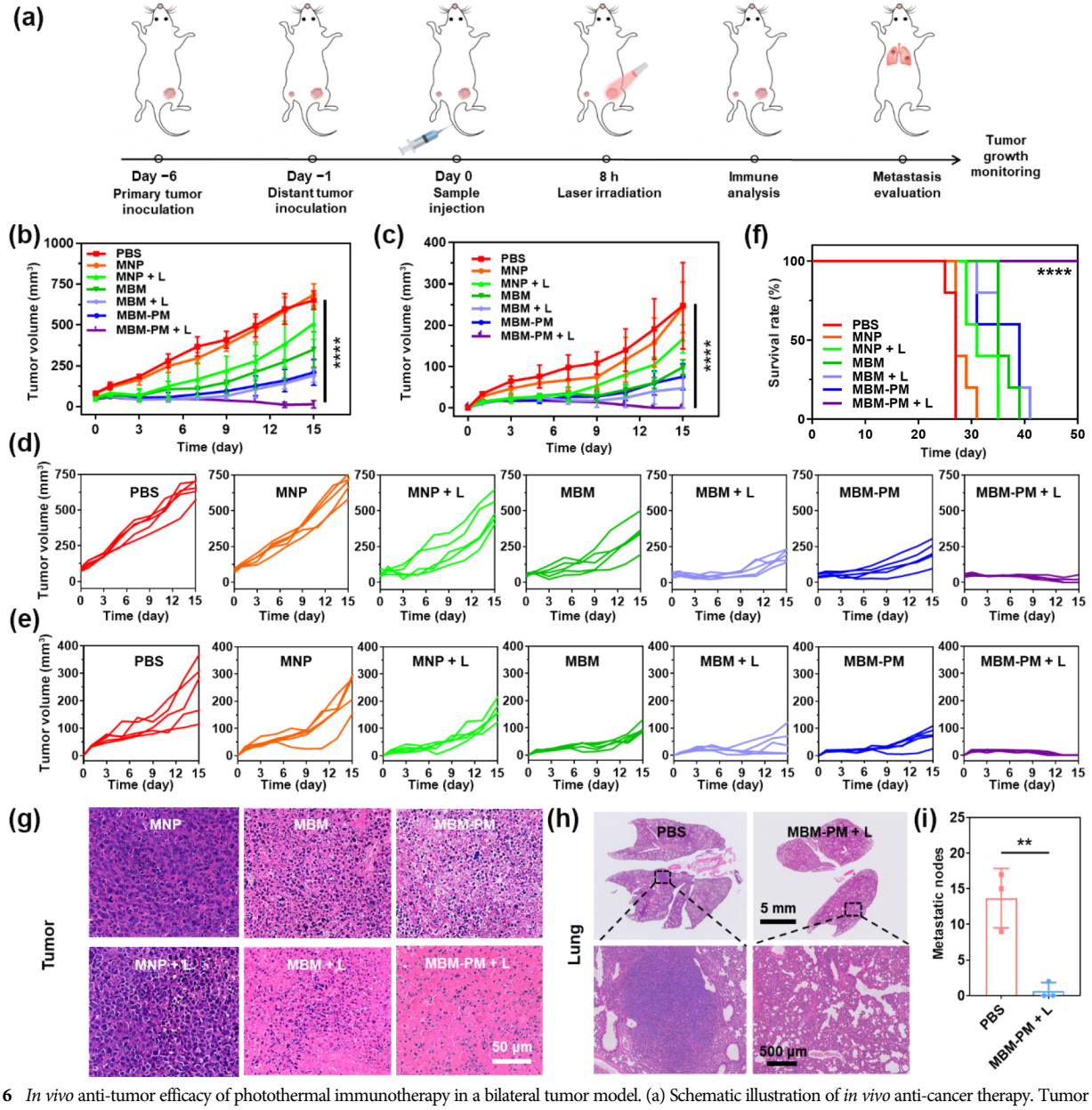

Figure 6 *In vivo* anti-tumor efficacy of photothermal immunotherapy in a bilateral tumor model. (a) Schematic illustration of *in vivo* anti-cancer therapy. Tumor growth curves of (b) primary and (c) distant tumors in mice after different treatments (n = 5). Individual tumor growth curves of (d) primary tumors and (e) distant tumors. (f) Survival curves of mice bearing bilateral 4T1 tumors after different treatments (n = 5). (g) Representative H&E-stained images of the primary tumors after different treatments. (h) Representative H&E-stained images of lung sections after different treatments. (i) Quantification of metastatic nodules per lung after different treatments (n = 3). Data were expressed as mean ± SD. Statistical significance in (b) and (c) was calculated via one-way ANOVA with a Tukey post-hoc test. Statistical significance in (f) was calculated via the log-rank test. Statistical significance in (i) was calculated via two-tailed Student's t-test. $^{**}P < 0.01$; $^{****}P < 0.0001$.

exhibited the most significant tumor-cell nuclear dissociation in H&E-stained images. Pulmonary metastasis of mice after treatment was examined on day 28 by H&E staining (Fig. 6(h)). In contrast to the PBS-treated group, which exhibited a significant number of metastatic nodules, the group treated with MBM-PM combined with laser irradiation showed almost no metastatic nodules (Fig. 6(i)). Taken together, we have demonstrated that the MBM-PM-mediated photothermal immunotherapy possessed desirable therapeutic efficacy to not only impeded growth of both primary and distant tumors, but also arrested systemic cancer metastasis to lung.

The biosafety profiles of MBM-PM were systematically evaluated to ensure the safety for bioapplication. First, the hemolysis rate was examined which was less than 2% when the concentration of MBM-PM was as high as 200 μg·mL^{-1} (Fig. S2 in the ESM). Moreover, no noticeable changes in body weights were found in any group of mice during the treatment period (Fig. S3 in the ESM). H&E staining images of major organs collected from mice receiving different treatments did not show observable damage or inflammation (Fig. S4 in the ESM). Additionally, kidney and liver functions of mice treated with MBM-PM showed no obvious abnormalities compared to the PBS group (Fig. S5 in the ESM). This indicated the good biosafety and biocompatibility of MBM-PM-mediated therapy.

3.5 *In vivo* mechanism studies of photothermal immunotherapy

To gain insights into the mechanisms of anti-tumor immune responses induced by MBM-PM injection in combination with PTT, we first evaluated DC activation in lymph nodes draining the tumors through flow cytometry analysis on day 3 after different treatments (Fig. S6 in the ESM). The percentage of matured DCs ($CD80^+CD86^+$) in the MBM-PM + laser irradiation group exhibited the highest increase among different treatments, which was 2.25-fold higher than that in the PBS group (Fig. 7(a)). The maturation of DCs could be responsible for more effective tumor antigen presentation, potentially contributing to the enhanced infiltration of intratumoral T cells. To further explore this effect, we evaluated the differences in the subpopulations of T cells in primary tumors on day 14 after different treatments (Fig. S7 in the ESM). Consistent with the DCs maturation results, the MBM-PM + laser irradiation group presented the most significant $CD8^+$ T cells, which were 1.7-fold higher than that in the PBS group (Fig. 7(b)). In addition to evaluating immune activator cells, we assessed the subpopulation of immune suppressor cells in primary and distant tumors on day 14 after different treatments, specifically tumor regulatory T cells (T_{regs}, $CD3^+CD4^+CD25^+Foxp3^+$) (Figs. 7(c) and 7(d), and Fig. S7 in the ESM). The percentages of T_{regs} ($CD4^+Foxp3^+$) in primary and distant tumors of the MBM-PM + laser irradiation group decreased by 31.9% and 61.7% compared to that of the PBS-injected mice. The decrease of T_{regs} likely further facilitated antitumor immunity by relieving the immune suppressive microenvironment. Besides, we also studied the development of long-term immunity by measuring the subpopulation of effector memory T cells (T_{em} cells, $CD3^+CD8^+CD44^+CD62L^-$) in spleens on day 14 after different treatments (Fig. S8 in the ESM). The group of mice treated with MBM-PM and laser irradiation showed a higher increase of T_{em} cells than other groups, which was 3.1-fold higher than the PBS group (Fig. 7(e)). The remarkable increase of T_{em} cells indicated a strong immune response, enhancing the body's ability to combat cancer cells effectively.

Expression levels of representative biomarkers, including those related to thermal stress (heat shock proteins 70 and 90, HSP70/90) and ICD (HMGB1 and CRT), as well as the extent of apoptosis (TUNEL), were assessed by immunofluorescent staining of primary tumor sections on day 3 (Fig. 8(a)). The results demonstrated that MBM-PM combined with laser irradiation treatment induced significant thermal stress, as evidenced by the substantial upregulation of HSP70 and HSP90. This increase in thermal stress markers was accompanied by a significant upregulation of CRT expression and the release of HMGB1, both of which are indicative

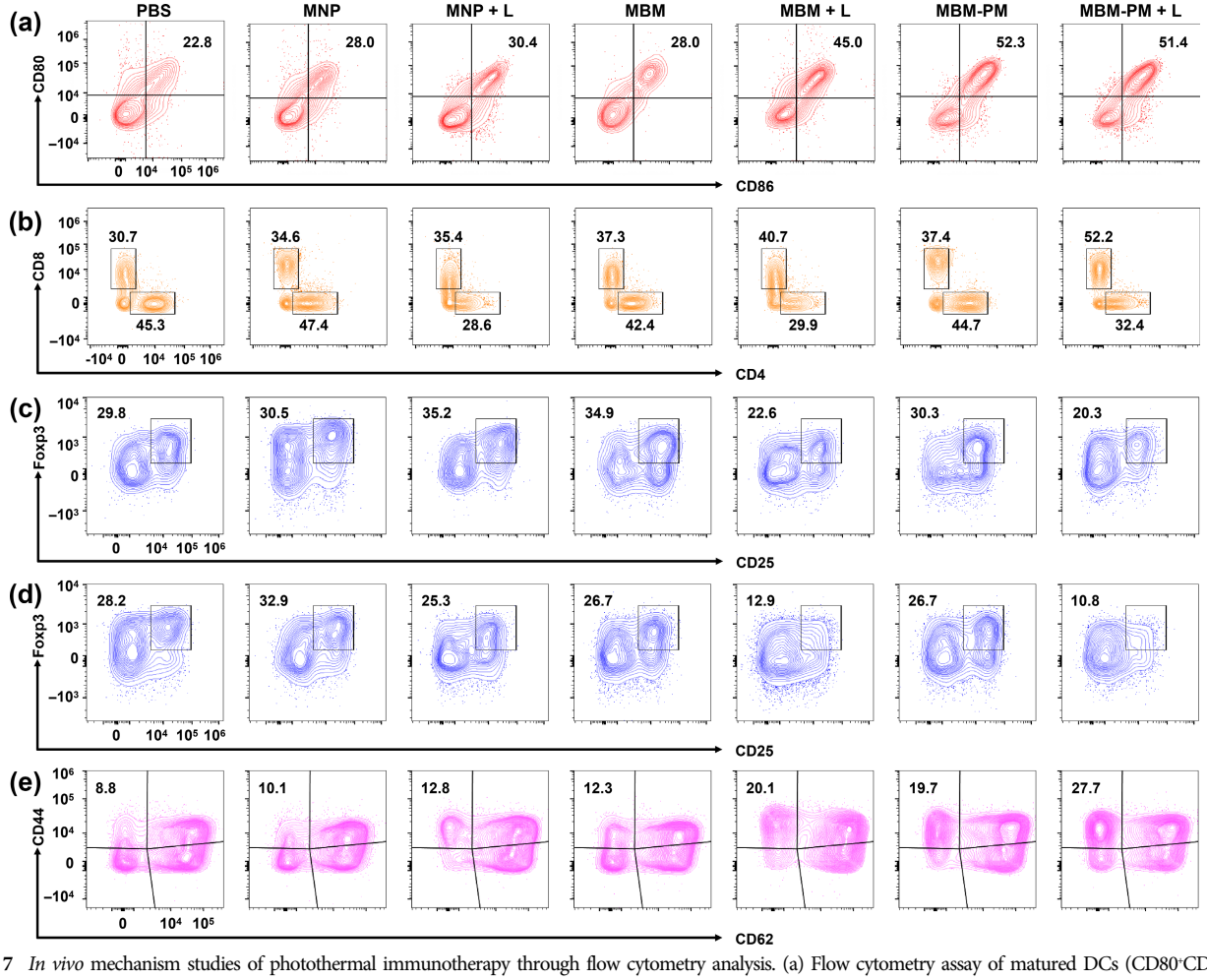

Figure 7 *In vivo* mechanism studies of photothermal immunotherapy through flow cytometry analysis. (a) Flow cytometry assay of matured DCs ($CD80^+CD86^+$) in TDLNs from 4T1 tumor-bearing mice on day 3 after different treatments. (b) Flow cytometry assay of tumor-infiltrating T lymphocytes ($CD8^+$ and $CD4^+$) in primary tumors. Flow cytometry assay of tumor regulatory T cells (T_{regs}, $CD3^+CD4^+CD25^+Foxp3^+$) in (c) primary tumors and (d) distant tumors on day 14 after different treatments. (e) Flow cytometry assay of effector memory T cells (T_{em} cells, $CD3^+CD8^+CD44^+CD62L^-$) in spleens on day 14 after different treatments.

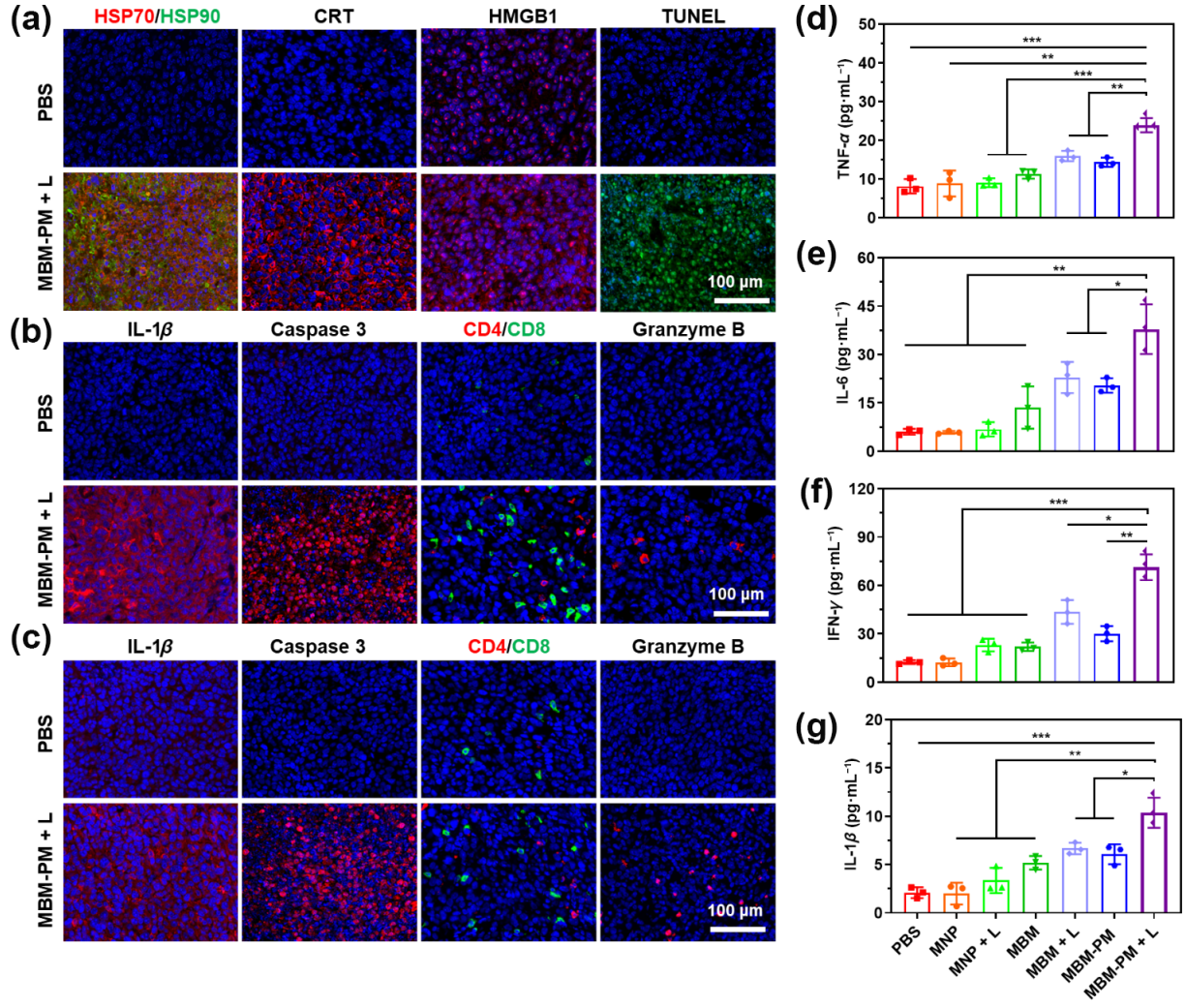

Figure 8 *In vivo* mechanism studies of photothermal immunotherapy through immunofluorescent staining and serum analysis. (a) Immunofluorescent images of HSP70 (red), HSP90 (green), CRT (red), HMGB1 (red) and TUNEL (green) in primary tumor sections on day 3 after different treatments. Immunofluorescent images of caspase-3 (red), IL-1β (red), CD4 (red), CD8 (green) and granzyme B (red) in (b) primary tumors and (c) distant tumors on day 14 after different treatments. Cell nuclei were stained with DAPI (blue). (d) TNF-α, (e) IL-6, (f) IFN-γ and (g) IL-1β levels in serum on day 3 after different treatments (n = 3). Data were expressed as mean ± SD. Statistical significance was calculated via two-tailed Student's t-test. *P < 0.05; **P < 0.01; ***P < 0.001; and ****P < 0.0001.

of ICD induction. Additionally, TUNEL staining revealed increased levels of apoptosis in the primary tumor sections, further confirming the efficacy of the combined treatment in promoting cell death.The expression levels of caspase-3 (a key executor of apoptosis), IL-1β (an inflammatory cytokine and endogenous immunity inducer [24]), CD4 (a marker of helper T cells), CD8 (a marker of cytotoxic T cells), and granzyme B (a serine protease involved in inducing apoptosis in target cells) in primary and distant tumors were analyzed respectively on day 14 to assess tumor growth inhibition and activation of the antitumor immune response via immunofluorescence imaging (Figs. 8(b) and 8(c)). Significant red fluorescence of caspase 3 was observed in the MBM-PM + laser irradiation group, indicating substantial cellular apoptosis following treatment. Additionally, IL-1β, an inflammatory cytokine and endogenous immunity inducer, was upregulated. The increased expression of CD4, CD8, and granzyme B suggests a robust activation of the immune response, not only in the primary tumors but also in distant tumors, highlighting the systemic antitumor effects and the potential of the treatment to target both local and metastatic sites. Moreover, the immunostimulatory cytokines including TNF-α, IL-6, IFN-γ and IL-1β in serum from the MBM-PM + laser irradiation group increased by 2.9-, 6.2-, 5.7- and 5.0-fold compared with the PBS-injected mice (Figs. 8(d)–8(g)). These data demonstrated that MBM-PM-mediated photo-immunotherapy could induce tumor ICD and elevate immunostimulatory cytokine levels to improve tumor immunogenicity and antitumor immune response.

4 Conclusions

In summary, we have developed a biosynthesized melanotic nanovesicles that can specifically targeted PD-L1-experssing cancer cells and induce cancer cell death through thermal stress and antitumor immune responses. The MBM-PM demonstrated robust efficacy in eradicating primary tumors, inhibiting distant tumors and preventing the spread of metastasis *in vivo*, highlighting its potential as a powerful tool in cancer treatment. This work provides a synthetic biology-driven strategy for further exploration and optimization of biosynthetic nanomedicines for cancer treatment.

Electronic Supplementary Material: Supplementary material (supporting figures as noted in the text; fluorescence images of the EGFP-PD-1-expressing cells; SDS-PAGE analysis, hemolysis test; body weight curves, representative H&E-stained images of major organs; blood biochemistry analysis; gating strategies for flow cytometry analysis; immunofluorescent images; and cytokine levels) is available in the online version of this article at https://doi.org/10.26599/NR.2026.94908589.

Data availability

All data needed to support the conclusions in the paper are presented in the manuscript and/or the Electronic Supplementary Material. Additional data related to this paper may be requested from the corresponding author upon request.

Acknowledgements

This work is financially supported by the National Key R&D Program of China (No. 2020YFA0908800), Basic Research Program of Shenzhen (No. KQTD20190929172538530), Shenzhen University 2035 Program for Excellent Research (Nos. 2023B006 and 2024C004), Research Team Cultivation Program of Shenzhen University (Nos. 2023QNT017 and 2023QNT019), and Program for Youzuzhikeyan of Shenzhen University (No. SZU2024YZZKY002). We thank Instrumental Analysis Center of Shenzhen University.

Declaration of competing interest

All the contributing authors report no conflict of interests in this work.

Author contribution statement

J. Y. Z. W.: Supervision, funding acquisition, writing – original draft. J. H. L.: Investigation, formal analysis, data validation, visualization, writing – original draft. M. W.: Methodology, investigation. P. J. M.: Investigation. H. K. L.: Methodology. J. L.: Conceptualization, supervision, funding acquisition, writing – review & editing. F. Y.: Conceptualization, supervision, funding acquisition, resources, writing – review & editing. P. H.: Conceptualization, supervision, funding acquisition, resources, writing – review & editing.

Informed consent

Not applicable.

Ethics statement

The animal experiments were conducted in accordance with the regulations of the Animal Ethical and Welfare Committee of Shenzhen University (AEWC-SZU, Ethics code: AEWC-202300010).

Use of AI statement

None.

References

[1] Couzin-Frankel, J. Breakthrough of the year 2013. *Cancer immunotherapy. Science* **2013**, *342*, 1432–1433.
[2] Mellman, I.; Coukos, G.; Dranoff, G. Cancer immunotherapy comes of age. *Nature* **2011**, *480*, 480–489.
[3] Hegde, P. S.; Chen, D. S. Top 10 challenges in cancer immunotherapy. *Immunity* **2020**, *52*, 17–35.
[4] Martin, J. D.; Cabral, H.; Stylianopoulos, T.; Jain, R. K. Improving cancer immunotherapy using nanomedicines: Progress, opportunities and challenges. *Nat. Rev. Clin. Oncol.* **2020**, *17*, 251–266.
[5] Park, J.; Wrzesinski, S. H.; Stern, E.; Look, M.; Criscione, J.; Ragheb, R.; Jay, S. M.; Demento, S. L.; Agawu, A.; Licona Limon, P. et al. Combination delivery of TGF-β inhibitor and IL-2 by nanoscale liposomal polymeric gels enhances tumour immunotherapy. *Nat. Mater.* **2012**, *11*, 895–905.
[6] Smyth, M. J.; Ngiow, S. F.; Ribas, A.; Teng, M. W. L. Combination cancer immunotherapies tailored to the tumour microenvironment. *Nat. Rev. Clin. Oncol.* **2016**, *13*, 143–158.
[7] Nam, J.; Son, S.; Park, K. S.; Zou, W. P.; Shea, L. D.; Moon, J. J. Cancer nanomedicine for combination cancer immunotherapy. *Nat. Rev. Mater.* **2019**, *4*, 398–414.
[8] Li, X. S.; Lovell, J. F.; Yoon, J.; Chen, X. Y. Clinical development and potential of photothermal and photodynamic therapies for cancer. *Nat. Rev. Clin. Oncol.* **2020**, *17*, 657–674.
[9] Galluzzi, L.; Buqué, A.; Kepp, O.; Zitvogel, L.; Kroemer, G. Immunogenic cell death in cancer and infectious disease. *Nat. Rev. Immunol.* **2017**, *17*, 97–111.
[10] Krysko, D. V.; Garg, A. D.; Kaczmarek, A.; Krysko, O.; Agostinis, P.; Vandenabeele, P. Immunogenic cell death and DAMPs in cancer therapy. *Nat. Rev. Cancer* **2012**, *12*, 860–875.
[11] Ng, C. W.; Li, J. C.; Pu, K. Y. Recent progresses in phototherapy-synergized cancer immunotherapy. *Adv. Funct. Mater.* **2018**, *28*, 1804688.
[12] Wu, J. Y.; Pu, K. Y. Leveraging semiconducting polymer nanoparticles for combination cancer immunotherapy. *Adv. Mater.* **2024**, *36*, 2308924.
[13] Ali, M. R. K.; Wu, Y.; Tang, Y.; Xiao, H. P.; Chen, K. C.; Han, T. G.; Fang, N.; Wu, R. H.; El-Sayed. M. A. Targeting cancer cell integrins using gold nanorods in photothermal therapy inhibits migration through affecting cytoskeletal proteins. *Proc. Natl. Acad. Sci. USA* **2017**, *114*, E5655–E5663.
[14] Tian, Q. W.; Tang, M. H.; Sun, Y. G.; Zou, R. J.; Chen, Z. G.; Zhu, M. F.; Yang, S. P.; Wang, J. L.; Wang, J. H.; Hu, J. Q. Hydrophilic flower-like CuS superstructures as an efficient 980 nm laser-driven photothermal agent for ablation of cancer cells. *Adv. Mater.* **2011**, *23*, 3542–3547.
[15] Han, B.; Zhang, Y. L.; Chen, Q. D.; Sun, H. B. Carbon-based photothermal actuators. *Adv. Funct. Mater.* **2018**, *28*, 1802235.
[16] Nam, J.; Son, S.; Ochyl, L. J.; Kuai, R.; Schwendeman, A.; Moon, J. J. Chemo-photothermal therapy combination elicits anti-tumor immunity against advanced metastatic cancer. *Nat. Commun.* **2018**, *9*, 1074.
[17] Yang, Y. Q.; Fan, X. X.; Li, L.; Yang, Y. M.; Nuernisha, A.; Xue, D. W.; He, C.; Qian, J.; Hu, Q. L.; Chen, H. et al. Semiconducting polymer nanoparticles as theranostic system for near-infrared-II fluorescence imaging and photothermal therapy under safe laser fluence. *ACS Nano* **2020**, *14*, 2509–2521.
[18] Wu, J. Y. Z.; Zhang, Y. F.; Jiang, K. J.; Wang, X. Y.; Blum, N. T.; Zhang, J.; Jiang, S. S.; Lin, J.; Huang, P. Enzyme-engineered conjugated polymer nanoplatform for activatable companion diagnostics and multistage augmented synergistic therapy. *Adv. Mater.* **2022**, *34*, 2200062.
[19] Chen, Q.; Xu, L. G.; Liang, C.; Wang, C.; Peng, R.; Liu, Z. Photothermal therapy with immune-adjuvant nanoparticles together with checkpoint blockade for effective cancer immunotherapy. *Nat. Commun.* **2016**, *7*, 13193.
[20] Chen, G. Y.; Roy, I.; Yang, C. H.; Prasad, P. N. Nanochemistry and nanomedicine for nanoparticle-based diagnostics and therapy. *Chem. Rev.* **2016**, *116*, 2826–2885.

[21] Jiang, J. W.; Huang, Y. J.; Zeng, Z. S.; Zhao, C. S. Harnessing engineered immune cells and bacteria as drug carriers for cancer immunotherapy. *ACS Nano* **2023**, 843–884.
[22] Cao, Z. P.; Liu, J. Y. Bacteria and bacterial derivatives as drug carriers for cancer therapy. *J. Control. Release* **2020**, *326*, 396–407.
[23] Kaparakis-Liaskos, M.; Ferrero, R. L. Immune modulation by bacterial outer membrane vesicles. *Nat. Rev. Immunol.* **2015**, *15*, 375–387.
[24] Liu, G. N.; Ma, N. N.; Cheng, K. M.; Feng, Q. Q.; Ma, X. T.; Yue, Y. L.; Li, Y.; Zhang, T. J.; Gao, X. Y.; Liang, J. et al. Bacteria-derived nanovesicles enhance tumour vaccination by trained immunity. *Nat. Nanotechnol.* **2024**, *19*, 387–398.
[25] Zhao, X.; Zhao, R. F.; Nie, G. J. Nanocarriers based on bacterial membrane materials for cancer vaccine delivery. *Nat. Protoc.* **2022**, *17*, 2240–2274.
[26] Kim, O. Y.; Park, H. T.; Dinh, N. T. H.; Choi, S. J.; Lee, J.; Kim, J. H.; Lee, S. W.; Gho, Y. S. Bacterial outer membrane vesicles suppress tumor by interferon-γ-mediated antitumor response. *Nat. Commun.* **2017**, *8*, 626.
[27] Li, J. J.; Xia, Q.; Guo, H. Y.; Fu, Z. Z.; Liu, Y.; Lin, S. S.; Liu, J. Y. Decorating bacteria with triple immune nanoactivators generates tumor-resident living immunotherapeutics. *Angew. Chem., Int. Ed.* **2022**, *61*, e202202409.
[28] Chen, Q.; Huang, G. J.; Wu, W. T.; Wang, J. W.; Hu, J. W.; Mao, J. M.; Chu, P. K.; Bai, H. Z.; Tang, G. P. A hybrid eukaryotic-prokaryotic nanoplatform with photothermal modality for enhanced antitumor vaccination. *Adv. Mater.* **2020**, *32*, 1908185.
[29] Peng, L. H.; Wang, M. Z.; Chu, Y.; Zhang, L.; Niu, J.; Shao, H. T.; Yuan, T. J.; Jiang, Z. H.; Gao, J. Q.; Ning, X. H. Engineering bacterial outer membrane vesicles as transdermal nanoplatforms for photo-TRAIL-programmed therapy against melanoma. *Sci. Adv.* **2020**, *6*, eaba2735.
[30] Qing, S.; Lyu, C. L.; Zhu, L.; Pan, C.; Wang, S.; Li, F.; Wang, J. H.; Yue, H.; Gao, X. Y.; Jia, R. R. et al. Biomineralized bacterial outer membrane vesicles potentiate safe and efficient tumor microenvironment reprogramming for anticancer therapy. *Adv. Mater.* **2020**, *32*, 2002085.
[31] Qin, H.; Chen, Y.; Wang, Z. M.; Li, N.; Sun, Q.; Lin, Y. X.; Qiu, W. Y.; Qin, Y. T.; Chen, L.; Chen, H. Q. et al. Biosynthesized gold nanoparticles that activate Toll-like receptors and elicit localized light-converting hyperthermia for pleiotropic tumor immunoregulation. *Nat. Commun.* **2023**, *14*, 5178.
[32] Lin, J.; Wang, M.; Hu, H.; Yang, X. Y.; Wen, B.; Wang, Z. T.; Jacobson, O.; Song, J. B.; Zhang, G. F.; Niu, G. et al. Multimodal-imaging-guided cancer phototherapy by versatile biomimetic theranostics with UV and γ-irradiation protection. *Adv. Mater.* **2016**, *28*, 3273–3279.
[33] Qi, C.; Fu, L. H.; Xu, H.; Wang, T. F.; Lin, J.; Huang, P. Melanin/polydopamine-based nanomaterials for biomedical applications. *Sci. China Chem.* **2019**, *62*, 162–188.
[34] Fu, M. J.; Yang, Y. P.; Zhang, Z. M.; He, Y. L.; Wang, Y. Y.; Liu, C. X.; Xu, X. H.; Lin, J.; Yan, F. Biosynthesis of melanin nanoparticles for photoacoustic imaging guided photothermal therapy. *Small* **2023**, *19*, 2205343.
[35] Zhang, X. D.; Wang, J. Q.; Chen, Z. W.; Hu, Q. Y.; Wang, C.; Yan, J. J.; Dotti, G.; Huang, P.; Gu, Z. Engineering PD-1-presenting platelets for cancer immunotherapy. *Nano Lett.* **2018**, *18*, 5716–5725.
[36] Zhang, X. D.; Wang, C.; Wang, J. Q.; Hu, Q. Y.; Langworthy, B.; Ye, Y. Q.; Sun, W. J.; Lin, J.; Wang, T. F.; Fine, J. et al. PD-1 blockade cellular vesicles for cancer immunotherapy. *Adv. Mater.* **2018**, *30*, 1707112.
[37] Zhang, Y. F.; Liao, Y. Y.; Tang, Q. N.; Lin, J.; Huang, P. Biomimetic nanoemulsion for synergistic photodynamic-immunotherapy against hypoxic breast tumor. *Angew. Chem., Int. Ed.* **2021**, *60*, 10647–10653.
[38] Gujrati, V.; Prakash, J.; Malekzadeh-Najafabadi, J.; Stiel, A.; Klemm, U.; Mettenleiter, G.; Aichler, M.; Walch, A.; Ntziachristos, V. Bioengineered bacterial vesicles as biological nano-heaters for optoacoustic imaging. *Nat. Commun.* **2019**, *10*, 1114.
[39] Jiang, S. S.; Li, W. Y.; Zhang, Y. F.; Lin, J.; Huang, P. Oxygen-regulated enzymatic nanoplatform for synchronous intervention in glycolysis and oxidative phosphorylation to augment antitumor therapy. *J. Control. Release* **2025**, *381*, 113594.
[40] Li, H. M.; Yin, D.; Li, W.; Tang, Q.; Zou, L.; Peng, Q. Polydopamine-based nanomaterials and their potentials in advanced drug delivery and therapy. *Colloids Surf. B: Biointerfaces* **2021**, *199*, 111502.
[41] Qi, X. L.; Huang, Y. J.; You, S. Y.; Xiang, Y. J.; Cai, E. Y.; Mao, R. T.; Pan, W. H.; Tong, X. Q.; Dong, W.; Ye, F. F. et al. Engineering robust Ag-decorated polydopamine nano-photothermal platforms to combat bacterial infection and prompt wound healing. *Adv. Sci.* **2022**, *9*, 2106015.
[42] Huang, L. P.; Li, Y. N.; Du, Y. N.; Zhang, Y. Y.; Wang, X. X.; Ding, Y.; Yang, X. L.; Meng, F. L.; Tu, J. S.; Luo, L. et al. Mild photothermal therapy potentiates anti-PD-L1 treatment for immunologically cold tumors via an all-in-one and all-in-control strategy. *Nat. Commun.* **2019**, *10*, 4871.
[43] Zhang, X.; Du, J. F.; Guo, Z.; Yu, J.; Gao, Q.; Yin, W. Y.; Zhu, S.; Gu, Z. J.; Zhao, Y. L. Efficient near infrared light triggered nitric oxide release nanocomposites for sensitizing mild photothermal therapy. *Adv. Sci.* **2019**, *6*, 1801122.
[44] Gao, G.; Sun, X. B.; Liang, G. L. Nanoagent-promoted mild-temperature photothermal therapy for cancer treatment. *Adv. Funct. Mater.* **2021**, *31*, 2100738.